

Article

Open Access



Ion transport, mechanical properties and relaxation dynamics in structural battery electrolytes consisting of an imidazolium protic ionic liquid confined into a methacrylate polymer

Achilleas Pipertzis¹, Nicole Abdou², Johanna Xu³ , Leif E. Asp³, Anna Martinelli² , Jan Swenson^{1,*} 

¹Department of Physics, Chalmers University of Technology, Gothenburg 41296, Sweden.

²Department of Chemistry and Chemical Engineering, Chalmers University of Technology, Gothenburg 41296, Sweden.

³Department of Industrial and Materials Science, Chalmers University of Technology, Gothenburg 41296, Sweden.

*Correspondence to: Prof. Jan Swenson, Department of Physics, Chalmers University of Technology, Gothenburg 41296, Sweden. E-mail: jan.swenson@chalmers.se

How to cite this article: Pipertzis A, Abdou N, Xu J, Asp LE, Martinelli A, Swenson J. Ion transport, mechanical properties and relaxation dynamics in structural battery electrolytes consisting of an imidazolium protic ionic liquid confined into a methacrylate polymer. *Energy Mater* 2023;3:300050. <https://dx.doi.org/10.20517/energymater.2023.49>

Received: 30 Jun 2023 **First Decision:** 2 Aug 2023 **Revised:** 4 Sep 2023 **Accepted:** 28 Sep 2023 **Published:** 7 Nov 2023

Academic Editors: Jiaqi Huang, Giovanni Battista Appetecchi **Copy Editor:** Fangling Lan **Production Editor:** Fangling Lan

Abstract

The effect of confining a liquid electrolyte into a polymer matrix was studied by means of Raman spectroscopy, differential scanning calorimetry, temperature-modulated differential scanning calorimetry, dielectric spectroscopy, and rheology. The polymer matrix was obtained from thermal curing ethoxylated bisphenol A dimethacrylate while the liquid electrolyte consisted of a protic ionic liquid based on the ethyl-imidazolium cation [C₂HIm] and the bis(trifluoromethanesulfonyl)imide [TFSI] anion, doped with LiTFSI salt. We report that the confined liquid phase exhibits the following characteristics: (i) a distinctly reduced degree of crystallinity; (ii) a broader distribution of relaxation times; (iii) reduced dielectric strength; (iv) a reduced cooperativity length scale at the liquid-to-glass transition temperature (T_g); and (v) up-speeded local T_g -related ion dynamics. The latter is indicative of weak interfacial interactions between the two nanophases and a strong geometrical confinement effect, which dictates both the ion dynamics and the coupled structural relaxation, hence lowering T_g by about 4 K. We also find that at room temperature, the ionic conductivity of the structural electrolyte achieves a value of 0.13 mS/cm, one decade lower than the corresponding bulk electrolyte. Three mobile ions (Im⁺, TFSI⁻, and Li⁺) contribute to the measured ionic conductivity, implicitly reducing the Li⁺ transference number. In addition, we report that the investigated solid polymer electrolytes exhibit the shear modulus needed for transferring the mechanical load to the carbon fibers in a structural battery. Based on these findings, we conclude that optimized



© The Author(s) 2023. **Open Access** This article is licensed under a Creative Commons Attribution 4.0 International License (<https://creativecommons.org/licenses/by/4.0/>), which permits unrestricted use, sharing, adaptation, distribution and reproduction in any medium or format, for any purpose, even commercially, as long as you give appropriate credit to the original author(s) and the source, provide a link to the Creative Commons license, and indicate if changes were made.



microphase-separated polymer electrolytes, including a protic ionic liquid, are promising for the development of novel multifunctional electrolytes for use in future structural batteries.

Keywords: Structural battery electrolyte, protic ionic liquid, ionic conductivity, relaxation dynamics, confinement

INTRODUCTION

Over the past decades, lithium (Li)-ion batteries have gained the market as the main power and energy storage systems in electrified transportation, a vital field for the realization of a sustainable and environmentally friendly society^[1,2]. To meet the emerging demands of longer driving ranges and faster charging rates, higher energy/power densities or higher energy-to-weight ratios are needed. The latter can be achieved by developing a “mass-less energy storage system”, also known as a structural battery, that consists of lightweight multifunctional materials^[3-8]. Such a structural battery is based on carbon fiber-reinforced polymer composites able to store electrical energy in load-bearing body parts, e.g., in the roof or in the body panel of a car, in the interior of an airplane, or in parts of electric ferries^[9-12]. In structural batteries, carbon fibers are used as a host for Li ions and for the conduction of electrons while also providing mechanical reinforcement. The matrix material in structural batteries not only supports ion transport but also enables transfer of mechanical load. By this design, the battery is simultaneously part of the structure and the source of power^[3-12].

One of the key challenges to achieving multifunctionality in structural batteries is the design of a suitable structural battery electrolyte (SBE), which simultaneously exhibits high Li-ion conductivity ($\sigma_{dc} > 1$ mS/cm) and enables mechanical load transfer to the carbon fibers^[13]. Since the pioneering study from 2007 by the US Army^[14], the scientific interest has turned to the design of novel microphase-separated heterogeneous structural electrolytes comprising two segregated phases: a glassy, rigid phase of a polymer matrix and a liquid ion-conducting phase that are independently responsible for the mechanical and the ion-conduction properties, respectively^[13-25]. In this context, Ihrner *et al.* established a phase-separated methacrylate-based SBE by a UV-cured synthetic method, in which the conductive phase consisted of an organic electrolyte^[15]. This system had an elastic modulus of about 360 MPa and an ionic conductivity of 0.2 mS/cm at ambient temperature^[15]. In a subsequent study^[16], it was evidenced that a thermal curing processing route was beneficial for the synthesis of phase-separated methacrylate-based SBE films and structural electrodes, yielding a combination of improved thermo-mechanical properties (up to 750 MPa) and electrochemical performance, similar to that found in UV-cured ones. Nevertheless, the use of organic solvents is accompanied by safety issues related to their flammability and volatility, increasing the risk of fire and explosion, hence limiting the temperature range of safe operation.

To alleviate the safety issues encountered with organic solvents, ionic liquids may be considered as part of the ion-conducting phase instead. Ionic liquids are salts composed mainly of organic ions that melt at low temperatures^[26-33]; they exhibit high thermal stability (low flammability), large electrochemical stability windows, and negligible vapor pressure. In the bulk phase, aprotic ionic liquids doped with a Li-salt exhibit higher conductivities than poly(ethylene oxide) (PEO)/LiTFSI polymer electrolytes but significantly lower than ethylene carbonate/LiTFSI electrolytes, reflecting the trend of viscosity^[32]. However, to advance the performance of ionic liquid-based materials, it is pivotal to understand their properties while confined into polymeric or inorganic matrices, materials also known as ionogels^[34-40].

The incorporation of ionic liquids into cross-linked polymer matrices, obtained by a synthetic method that induces phase separation, can result in high ionic conductivities at ambient temperature without sacrificing

the required mechanical strength, as first evidenced by Matsumoto *et al.*^[21]. Specifically, a micro-separation between 1-ethyl-3-methylimidazolium bis(trifluoromethanesulfonyl)imide ($[\text{C}_2\text{C}_1\text{Im}][\text{TFSI}]$) and the solid (cross-linked epoxy resin based on bisphenol A) phase and a good combination of ionic conductivity and Young's modulus were revealed for ionic liquid contents above 40 wt.%^[21]. Concomitantly, Shirshova *et al.* reported a clear correlation between the morphology, ionic conductivity, and mechanical performance of ionic liquid ($[\text{C}_2\text{C}_1\text{Im}][\text{TFSI}]$)-epoxy resin structural electrolytes, which can be further engineered by the type and the composition of the epoxy resin^[22]. An optimum ionic liquid composition of 70 wt.% was revealed, which yielded a room temperature conductivity of 0.8 mS/cm and Young's modulus of 0.2 GPa, reflecting a long characteristic length scale of each structure (spinodal microstructure)^[22]. In a subsequent work^[23], a strong effect of the Li-salt concentration on ionic conductivity was evidenced, the latter changing by about two orders of magnitude. Further, Yu *et al.* reported an ionic conductivity of 0.1 mS/cm and a tensile modulus of 200 MPa in SBEs comprising a solid phase based on an epoxy resin and a liquid ion-conducting phase based on mixing an aprotic ionic liquid ($[\text{C}_2\text{C}_1\text{Im}][\text{TFSI}]$) with an organic solvent [propylene carbonate (PC)]^[24]. Moreover, Kwon *et al.* recently studied a novel SBE based on an epoxy combined with the aprotic ionic liquid $[\text{C}_2\text{C}_1\text{Im}][\text{TFSI}]$ doped with LiTFSI (including the inorganic filler Al_2O_3), reporting an excellent ionic conductivity of 0.29 mS/cm and Young's modulus of 1.0 GPa, at 298 K^[25]. However, this system exhibited inherent brittleness and high cost, limiting the appeal for applications in energy storage devices^[25]. To overcome these limitations, protic ionic liquids (PILs) could be used instead. Along with providing similar physico-chemical properties to those of their aprotic analogs, PILs are cheaper and, in theory, more straightforward to synthesize^[41]. Importantly, previous works have already demonstrated that electrolytes for use in Li-ion batteries can be designed to be based on PILs^[42]. Also, a molecular dynamics (MD) simulations study proved that an ammonium-based PIL could be a better Li-ion conducting electrolyte than its aprotic counterpart^[32]. These results give reasons to believe that PILs can emerge as promising materials for inclusion in SBEs. Nevertheless, for an optimized use, a deeper understanding of the effect of confinement into a polymeric matrix is needed.

The effect of hard confinement on the dynamics of small molecules (i.e., water and other hydrogen bonded liquids and ionic liquids) and polymers has been of great scientific interest^[43-55]. In confinement, there are two competing factors that determine the relaxation dynamics: (i) surface interactions; and (ii) geometrical confinement. The former factor tends to dominate at higher temperatures, causing a slowing down of the dynamics, compared to the bulk. On the other hand, the impact of geometrical confinement is stronger at lower temperatures, in the vicinity of the glass transition temperature (T_g), and tends to speed up viscosity-related relaxation dynamics, thus lowering T_g , as compared to the bulk^[45,54,55]. There are several possible explanations for why geometrical confinement generally speeds up the local dynamics. One potential cause is that the liquid molecules have difficulties being equally packed as in the bulk liquid, causing the free volume to increase with the result of faster dynamics. Another explanation can be that the cooperativity length decreases, which also makes it easier for the molecules to move. To understand how the viscosity-related dynamics can be enhanced in confinement, it is important to elucidate how the T_g and the associated relaxation dynamics are altered.

Herein, we present the investigation of the thermodynamic phase diagram, ion conduction, relaxation dynamics, and mechanical properties for a series of SBEs comprising a glassy phase derived from EBPADMA and an ion-conducting phase based on the PIL ethylimidazolium bis(trifluoromethanesulfonyl)imide, abbreviated as $[\text{C}_2\text{HIm}][\text{TFSI}]$, doped with the salt LiTFSI. Properties are investigated by employing differential scanning calorimetry (DSC)/temperature-modulated (TM)-DSC, dielectric spectroscopy, rheology, and Raman spectroscopy. We report that upon incorporation into the polymer matrix, the crystallinity of the liquid phase significantly reduces, and the local dynamics speed up

(lower T_g), indicating weak interfacial interactions and a favorable geometrical confinement effect. Doping with the Li-salt further destabilizes the crystalline order but slightly increases T_g due to stronger ionic interactions that increase viscosity. To summarize, we find that the maximum room temperature ionic conductivity for the SBE doped with LiTFSI is as high as 0.13 mS/cm, only one decade lower than the corresponding bulk liquid phase. The reduced conductivity can be explained by non-perfect connectivity of the liquid phase, and improvements will be needed to reach the desired and targeted conductivity of about 1 mS/cm. Further, the SBEs investigated here exhibit an elastic behavior at ambient temperature with a shear storage modulus higher than 0.2 GPa, at 318 K. To conclude, this thorough work reports the impact of confining an ion-conducting liquid phase into a polymer matrix and how this confinement affects the thermodynamic properties, the ionic conductivity, and the relaxation dynamics. Overall, our results indicate that SBEs consisting of a methacrylate-based polymer and an ion conducting PIL can emerge as a promising material concept to realize multifunctional solid electrolytes for use in structural batteries.

EXPERIMENTAL

Materials

The PIL 1-Ethylimidazolium bis(trifluoromethylsulfonyl)imide [C_2 HIm][TFSI], 98% purity, was purchased from Iolitec. The monomer ethoxylated bisphenol A dimethacrylate (EBPADMA, M_w 540 g/mol) was provided by Sartomer (Arkema Group). The salt lithium bis(trifluoromethane)sulfonimide (LiTFSI) and the thermal initiator 2,2'-azobis(2-methylpropionitrile) (AIBN) were purchased from Sigma-Aldrich. All chemicals were used as received without further treatment. The chemical structure of these compounds is shown in [Figure 1](#).

Synthesis

SBEs derived from the monomer EBPADMA and the liquid mixture [C_2 HIm][TFSI]/LiTFSI were all prepared inside a N_2 filled glovebox (MBRAUN UNILab Plus Eco glovebox with an MB-LMF II solvent absorber system; < 1 ppm H_2O ; < 1 ppm O_2). The liquid phases were prepared first by mixing LiTFSI with the PIL [C_2 HIm][TFSI] at different salt concentrations, i.e., 0.0, 0.1, and 0.2 m. As for the labeling of samples, a solid polymer electrolyte based on EBPADMA and a [C_2 HIm][TFSI]/LiTFSI solution with a concentration of 0.2 m is labeled EBPADMA + [C_2 HIm][TFSI]/LiTFSI_{0.2}.

For the synthesis of these polymer electrolytes, the [C_2 HIm][TFSI]/LiTFSI solution was first mixed with the monomer and with the thermal initiator AIBN in a glass vial. The AIBN content was 1 wt.% relative to the monomer. The liquid electrolyte content was kept equal to 50 wt.% of the total weight. This mixture of chemicals was then stirred using a vortex apparatus until a homogeneous solution was obtained. The mixture was then left to rest for 20 min in order to make all air bubbles escape.

As a second step, the prepared solution was poured onto a borosilicate petri dish. Then, the petri dish was inserted into a zipped bag and let cure over a metallic plate inside the glovebox, setting the temperature at 75 °C and letting cure for 180 min. During curing, polymerization occurs. The image of a defect-free solid polymer electrolyte obtained by this procedure is shown in [Figure 2A](#), while the chemical structure after polymerization is illustrated in [Figure 2B](#).

Thermogravimetric analysis

Thermogravimetric analysis (TGA) experiments were performed on a Mettler Toledo TGA/DSC3+ equipped with an autosampler. A XS105 semi-micro balance from Mettler Toledo was used to weigh the samples. A small amount of sample (~20 mg) was placed inside a 70 L aluminum crucible capped with an aluminum lid with a pinhole. The samples were then measured under air flow (60 L/min) from 25 to 800 °C at a heating rate of 10 K/min.

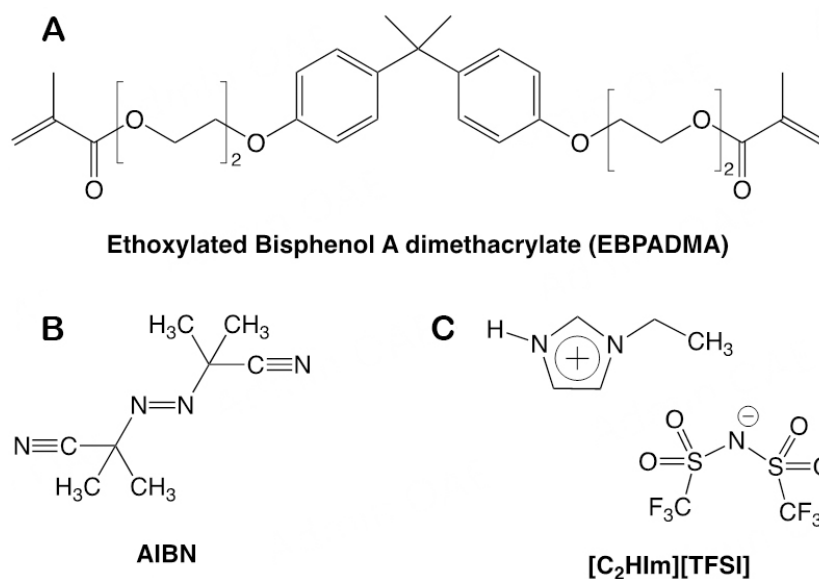


Figure 1. Chemical structure of the used compounds: (A) the methacrylate-based monomer; (B) the initiator; and (C) the protic ionic liquid.

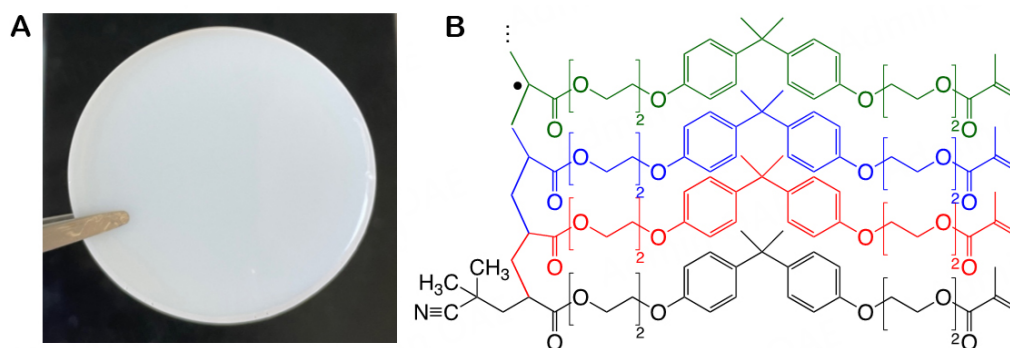


Figure 2. (A) Picture of the solid polymer electrolyte EBPADMA + [C₂HIm][TFSI]/LiTFSI_{0.2} and (B) sketch of the radical polymerization of EBPADMA monomers.

Scanning electron microscopy

Scanning electron microscopy (SEM) images were taken using a Zeiss Ultra 55 FEG microscope. The studied samples were gold coated before the analysis using Leica EM TXP equipment. The diameter of the gold nanoparticles used is about 6 nm. Before collecting the SEM images, the ionic liquid was extracted with ethanol using a Soxhlet apparatus for 24 h.

Nitrogen sorption

Nitrogen sorption isotherms were recorded at 77 K using a Micromeritics TriStar volumetric apparatus by adding doses of N₂ in a measurement cell after an outgassing treatment of the extracted samples at 80 °C under mild vacuum overnight. The samples were extracted with ethanol using a Soxhlet apparatus for 24 h. The Brunauer-Emmett-Teller (BET) surface area of each sample was determined using the BET method in the linear range of the isotherms, typically at $p/p_0 = 0.05-0.15$ ^[56]. The pore size distribution was calculated using the Barret-Joyner-Halenda (BJH) method from the adsorption isotherm^[57]. The total pore volume of the materials was determined at $p/p_0 = 0.99$.

Calorimetric measurements

DSC measurements were performed for the determination of phase transition temperatures in the investigated electrolytes by employing a Q2000 (TA Instruments) setup equipped with a liquid nitrogen cooling system (LNCS). The temperature protocol involves a cooling scan to 153 K followed by a heating scan to 333 K, both at a rate of 10 K/min and under nitrogen flow. This procedure was repeated twice, with reproducible results. The T_g and the melting temperature (T_m) were analyzed in the heating scan of the second cycle. The instrument was calibrated for best performance in the specific temperature range and for the used heating/cooling rates. Pre-calibration procedures included (i) cleaning the cell; (ii) conditioning the cell (making an inert atmosphere by employing helium gas); and (iii) performing a LNCS baseline calibration. The main zero calibration sequence included a baseline calibration for the determination of the time constants and capacitances of the sample and reference sensor using a sapphire standard. In the subsequent step, an indium standard ($\Delta H = 28.71$ J/g, $T_m = 428.8$ K, with a heating rate of 10 K/min) was employed for the calibration of enthalpy and transition temperatures. Finally, a baseline measurement was done with an empty cell to verify the successful calibration of the instrument. Concerning the heat capacity calibration, a TM-DSC calibration was made with a sapphire standard. Samples with masses of 10-14 mg were encapsulated in hermetic aluminum pans using a sealing press and placed on the sample sensor. As a reference, an empty aluminum pan was used.

In addition to standard DSC, TM-DSC measurements were carried out to identify the dynamic nature of the confined liquid phase. The measurements were performed, covering the temperature range from 163 to 223 K. In TM-DSC, a low-frequency sinusoidal perturbation is added to the standard DSC profile, according to $T = T_0 + \beta t + AT\sin(\omega t)$, where β is the linear heating rate, t the time, A_T the amplitude, and ω the angular frequency^[58,59]. An amplitude of 1 K and periods in the range from 40 to 200 s were applied. The linear heating rate for each period of modulation was calculated from $\beta = (\Delta T/n\pi)60$ s/min, where ΔT is the temperature width of the glass “transition” (between the “onset” and “end” temperature), n is the number of modulation cycles ($n = 6$), and π is the period of modulation. By assuming a width of T_g of around 10 K, linear heating rates from 5 to 0.5 K/min were employed.

Dielectric spectroscopy

Dielectric measurements were performed using a Novocontrol GmbH broadband dielectric spectrometer, covering the frequency range 10^{-2} - 10^7 Hz. The solid electrolytes were painted with silver paste for good contact with the two stainless-steel electrodes (5 and 10 mm in diameter). The diameter of the silver-pasted area (ranging from 7 mm to 9 mm for the different samples) and the sample thickness (ranging from 700 to 900 μm in the different samples) were measured with a Mitutoyo absolute digital caliper. For the liquid electrolytes, the liquid parallel plate sample cell (BDS 1308) was employed with stainless steel electrodes (20 mm diameter). Teflon spacers were used to maintain a uniform thickness of 100 μm . Measurements were conducted in a temperature range between 173 K and 393 K in steps of 5 K, with a stabilization time of 600 s at each temperature. A low-voltage electric field of 0.01 V was employed to reduce electrode polarization effects. The temperature was controlled using a nitrogen gas cryostat, with stability of ± 0.1 K. At each measurement, the complex conductivity function, σ^* , the complex dielectric permittivity, $\varepsilon^*(\omega)$, and the complex electric modulus, $M^*(\omega)$, were recorded. In general, these are related according to the following equation:

$$\sigma^*(\omega) = i\omega\varepsilon_0\varepsilon^*(\omega) = \frac{i\omega\varepsilon_0}{M^*(\omega)} \quad (1)$$

where ω is the angular frequency, and ε_0 is the permittivity of free space.

Rheology

A MCR 302 rheometer by Anton Paar was employed for the measurements of the shear modulus in structural electrolytes. A plate-plate geometry with a diameter of 8 mm was used. The samples were prepared on the lower rheometer plate. Then, the upper plate was brought into contact, and the thickness was adjusted. Temperature control was achieved within ± 0.1 K with a cooling circulator provided by Anton Paar. Two types of measurements (in an oscillatory mode) were carried out in the linear viscoelastic regime: (i) temperature ramps under isochronal conditions ($\omega = 10$ rad/s) at the temperature range between 313 and 383 K; and (ii) frequency sweeps within the range $10^{-1} < \omega < 10^2$ rad/s, under isothermal conditions at 318 K ($T < T_g^{\text{EBPADMA}}$) and at 373 K ($T > T_g^{\text{EBPADMA}}$). The linear and nonlinear viscoelastic regions were identified through the strain amplitude dependence of the complex shear modulus, $|G^*(\omega)|$, at $\omega = 10$ rad/s.

Raman spectroscopy

Raman spectra were collected at room temperature using a Renishaw InVia Reflex Raman spectrophotometer equipped with an air-cooled CCD detector. A 785 nm wavelength diode laser was used as the excitation source, while the grating used had 1,200 grooves/mm. The Raman spectra of the ionic liquid and salt mixtures were collected at room temperature, covering the 100–4,000 cm^{-1} spectral range and keeping the samples inside sealed NMR tubes. The samples were loaded inside a glovebox. The Raman spectra of SBEs were collected from self-standing samples in air, also at room temperature. The laser power was set to 10% of its maximum value, which is about 300 mW at the source. Raman spectra are the result of ten accumulations with ten seconds of acquisition time each. Before each measurement, the spectrophotometer was calibrated to the first-order vibrational mode of a Si wafer centered at 520.6 cm^{-1} . The raw Raman spectra were treated by excluding sharp signals coming from cosmic rays. For further analysis and to estimate integrated areas, a multipeak fit procedure based on a linear background and Voigt functions was applied using the Igor Pro 9 software. In the fitting procedure, the width and position of the Voigt components were not subjected to any constraints.

RESULTS AND DISCUSSION

Thermal properties and morphology

The TGA results show that the pure PIL decomposes in two consecutive steps, the first one starting at around 300 °C. Upon confinement, the first step shifts to slightly lower temperatures, and an additional feature is observed, which is attributed to the decomposition of the polymer, see [Supplementary Figure 1](#).

A representative, cross-section SEM image of sample EBPADMA + [C₂HIm][TFSI]/LiTFSI_{0.2} is shown in [Figure 3A](#). After the extraction of the ionic liquid, the polymer phase shows an interconnected pore architecture with a wide pore size distribution (from micro- to macropores). Additional SEM images taken on the surface of the samples are available in the [[Supplementary Figure 2](#)].

Additionally, nitrogen sorption isotherms of the EBPADMA + [C₂HIm][TFSI] and EBPADMA + [C₂HIm][TFSI]/LiTFSI_{0.2} samples reveal that both studied materials have the same textural properties in terms of BET surface area (~ 40 m^2/g) and average pore size (i.e., pore volume at $p/p_0 = 0.99$ and average pore diameter calculated using BJH method upon adsorption), independently of the concentration of LiTFSI salt. Both materials show type IV(a) isotherms with a hysteresis loop of type H₃, [Figure 3B](#). These isotherms are characteristics of well-connected pores; moreover, the pore size distribution is wide, with an average BJH adsorption pore size of around 8 nm, see the inset of [Figure 3B](#).

These results highlight the interconnected porosity of the studied SBEs displaying a wide range of pore sizes. However, as discussed below, some pores have dead-ends that cannot be measured by nitrogen sorption measurements. Moreover, as clearly seen in [Figure 3](#), some of the pores observed in SEM are much larger

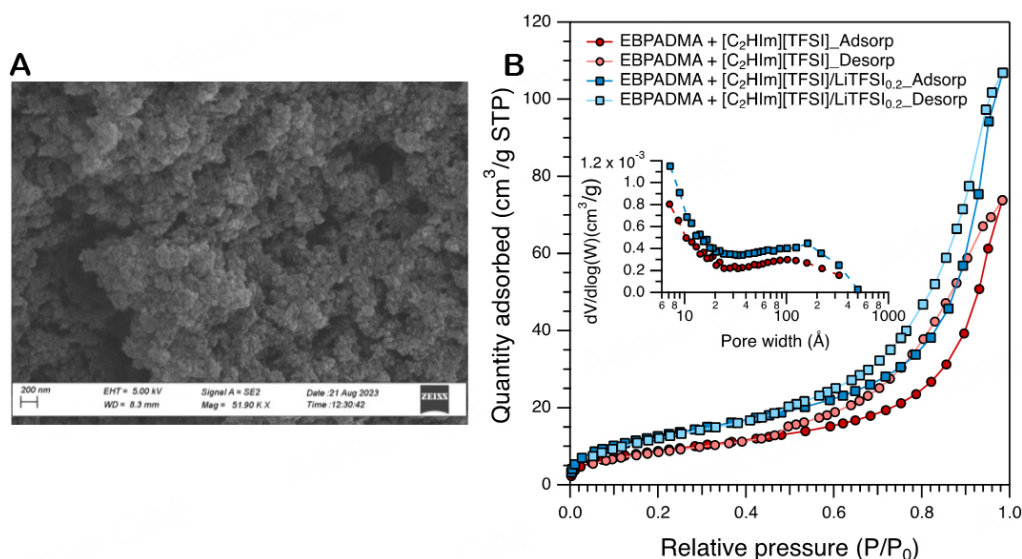


Figure 3. (A) SEM image of the cross-section of sample EBPADMA + [C₂HIm][TFSI]/LiTFSI_{0.2} with 200 nm scale bar. (B) Nitrogen sorption isotherms of EBPADMA + [C₂HIm][TFSI] (red circles) and EBPADMA + [C₂HIm][TFSI]/LiTFSI_{0.2} (blue squares) samples. The inset shows the BJH adsorption pore distribution of both studied samples.

than those measured by nitrogen sorption analysis (a technique that does not detect macro-pores larger than a few hundred nanometers).

Thermodynamics - phase diagram

Upon confinement of the bulk PIL into the structure of a polymer matrix, the temperatures of the first order transitions, the degree of crystallinity, and the T_g associated with the amorphous part of the liquid phase can be affected. DSC and TM-DSC calorimetric measurements were carried out for the EBPADMA-based solid electrolytes and their respective bulk PILs to estimate these changes, as summarized in [Figure 4](#).

As illustrated in [Figure 4](#), the confinement of the bulk PIL into the cured polymer distinctly affects the thermodynamic properties. The DSC traces of the solid electrolytes exhibit two liquid-to-glass temperatures, T_g s, indicating segregation between the ion-conducting liquid phase and the solid phase. The lower T_g is associated with the vitrification of the amorphous part of the ionic liquid, while the higher T_g is linked to the vitrification of the cross-linked glassy polymer matrix. The chemico-physical cross-linking of the polymer matrix via thermal curing results in a broad T_g (at ~ 360 K) with a width of about 50 K. Also, in the temperature range between the two T_g s, a cold crystallization exothermic peak at $T_{cc} \sim 230$ K, followed by a melting peak at ~ 278 K, can be observed. This decreases by about 5-10 K compared to the bulk phase as an effect of geometrical confinement and in accordance with the literature^[54]. However, in contrast to the case of the bulk liquid phase, for which the cold-crystallization (melting) temperature increases (decreases) with increasing Li-salt concentration, the first order transitions for the confined PIL are relatively unaffected by the Li-salt content. The temperatures of the first order phase transitions and the corresponding change of enthalpy are provided in [Supplementary Table 1](#) as well as in [Figure 4C](#) and [D](#), the orange and green arrows guiding through the effect of confinement and of increasing Li-salt concentration, respectively. As expected, the degree of crystallinity significantly reduces upon confinement of the liquid phase into the polymer. More specifically, the enthalpy change of fusion decreases by about 30 J/g in EBPADMA + [C₂HIm][TFSI] compared to the corresponding bulk ionic liquid. Further destabilization of the crystalline order is induced by adding Li-salt due to increased ionic interactions [[Figure 4C](#)]. Parenthetically, as it has been shown previously in the literature, the doping of Li-salt has a significant impact on the degree of crystallinity of the

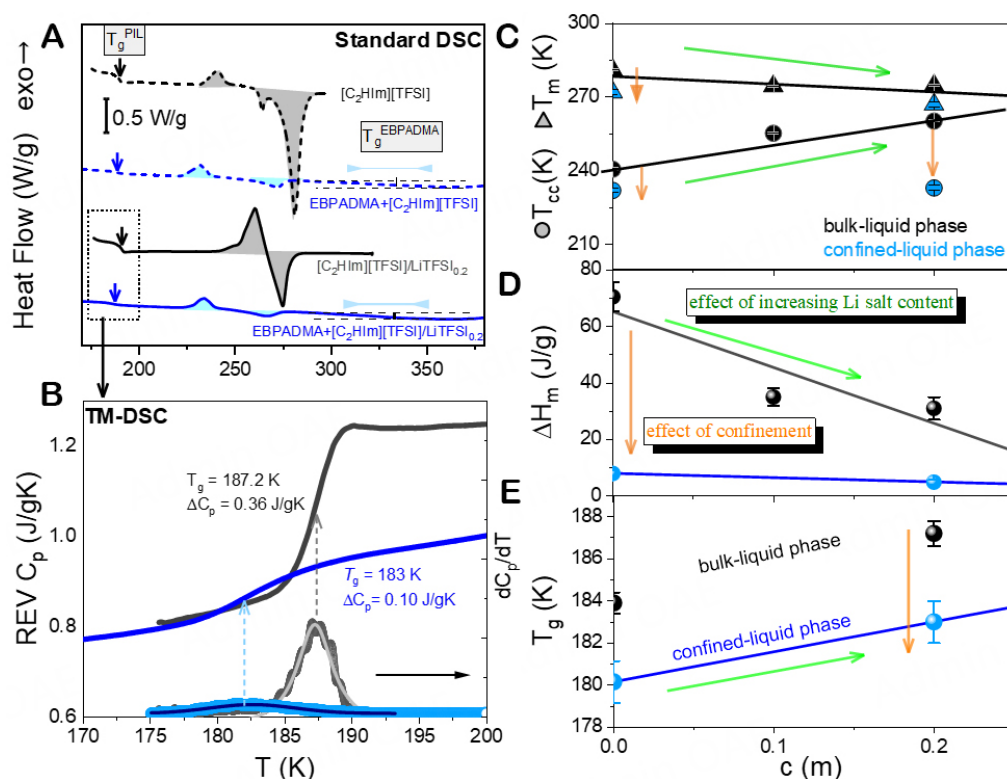


Figure 4. (A) DSC thermograms of the EBPADMA + [C₂HIm][TFSI]/LiTFSI electrolytes (blue) and their corresponding liquid electrolytes [C₂HIm][TFSI]/LiTFSI (black), with a Li-salt concentration equal to either 0.0 m (dashed lines) or 0.2 m (solid lines). The DSC traces shown are those recorded during the second heating at a rate of 10 K/min. The thermograms are vertically offset for clarity. (B) Reversing heat capacity as a function of temperature for samples [C₂HIm][TFSI]/LiTFSI_{0.2} (black) and EBPADMA + [C₂HIm][TFSI]/LiTFSI_{0.2} (blue), by employing TM-DSC with a period of 200 s and a linear heating rate of 0.5 K/min. Li-salt concentration dependence of (C) the crystallization and melting temperatures, (D) the enthalpy of fusion, and (E) the liquid-to-glass temperature, estimated from TM-DSC measurements ($P = 200$ s, $\beta = 0.5$ K/min) for the bulk liquid phase (black symbols) and the liquid phase inside the polymer (blue symbols). The arrows guide through the effect of increasing the Li-salt content (green arrows) and confinement (orange arrows). (C-E) The lines are simple guides to the eyes.

bulk liquid phase, and this is also verified by our results. Hence, the degree of crystallinity of PILs can be fine-tuned by (i) confinement into a polymer matrix; and (ii) doping with a Li-salt, yielding an almost amorphous environment that is favorable for the transport of Li ions.

Moreover, the incorporation of the liquid phase into the polymer matrix has a strong impact on the glassy state of the confined liquid phase, as can be observed in the TM-DSC thermograms. As shown in Figure 4B and E and in Supplementary Table 1, the T_g of the liquid phase decreases by about 4 K upon confinement, indicative of weaker interfacial interactions between the liquid and the solid phase. This suggests that the viscosity of the PIL decreases in confinement. Moreover, the change of heat capacity decreases by about 30% (1/3), reflecting the effect of confinement and the reduced degree of freedom compared to the bulk liquid phase [Figure 4B and Supplementary Figure 3]. On the other hand, doping with Li-salt slightly increases T_g by about 3 K, following a trend similar to that observed in the bulk liquid phase. This reflects stronger ionic interactions, which increase the liquid viscosity and thus raise T_g . However, the T_g of the doped confined PIL is still lower in confinement, implying overall weak interfacial interactions and a strong geometrical impact, as is discussed in more detail below with respect to the relaxation dynamics and the dynamic nature of T_g . Before delving deeper into such a discussion, we first present results on the chemical composition and the intermolecular interactions established in the proposed SBEs. Additionally,

we investigate the effects of confinement and Li-salt doping on the macroscopically measured ionic conductivity and mechanical properties.

Chemical homogeneity and intermolecular interactions

By Raman spectroscopy, the actual chemical composition of the synthesized solid polymer electrolytes and the nature of established intermolecular interactions were investigated. A selection of Raman spectra collected from the precursor monomer, the neat PIL, and the SBEs after curing are shown in [Figure 5](#).

First of all, the degree of curing was analyzed by investigating the intensity change of the Raman active mode arising from C=C stretching ($1,640\text{ cm}^{-1}$) with reference to the intensity of the C-C stretching mode ($1,610\text{ cm}^{-1}$) of the phenyl group that is not taking part in the polymerization reaction, see the inset of [Figure 5](#)^[60]. In fact, the intensity of the C=C mode at $1,640\text{ cm}^{-1}$ decreases with respect to the phenyl group mode as a consequence of polymerization, and from the analysis of the integrated areas under these peaks, we estimate a conversion value of about $86 \pm 0.4\%$ (the error is associated with the accuracy of the fitting of the integrated Raman intensities). The latter was also calculated from the DSC thermogram by employing a non-isothermal method and integrating the exothermic peak (found at $T \sim 400\text{ K}$) associated with the polymerization (curing) of residual monomers [[Supplementary Figure 4](#)]. A conversion value of $94\% \pm 2\%$ was estimated, a value slightly higher than that found from Raman spectroscopy but reasonably close. This value is the same for the samples prepared with and without the addition of the Li-TFSI salt and is also in agreement with values previously reported for equivalent materials, although analyzed by means of infrared spectroscopy^[16].

The lower spectral range between 240 and 450 cm^{-1} includes vibrations that are sensitive to conformational changes. As already discussed in the literature, the TFSI anion can adopt the *cis* or the *trans* conformation, each contributing with distinct but energetically close Raman intensities^[31]. The collected Raman spectra shown in [Figure 5](#) indicate the co-existence of both conformations, although we did not further investigate this region to quantitatively estimate the population of each of those.

The synthesized solid polymer electrolytes were also investigated to get insights into their homogeneity from a chemical composition point of view. For this purpose, Raman spectra were collected at arbitrarily selected spots on both sides of the material (top and bottom sides) and along a line cross-sectioning the thickness, as shown in [Figure 6A](#). The Raman spectra collected in this way look identical [[Supplementary Figures 5-7](#)], confirming that the relative amount of liquid and solid phases is constant across the material and that concentration gradients are not formed during curing (in particular, not top-to-bottom). The synthesized solid polymer electrolytes can, hence, be considered to be chemically homogeneous.

Another very important aspect that we have investigated is the nature of interactions established between the ionic species present in the liquid mixture, both in the bulk liquid and after confinement into the polymer matrix. Such interactions are typically investigated by analyzing the frequency of the expansion-contraction mode of TFSI, a strong Raman mode that is typically found in the range $741\text{-}744\text{ cm}^{-1}$ for weakly coordinated TFSI anions, e.g., in neat protic and aprotic ionic liquids based on the TFSI anion, in the liquid state^[61-63]. By a thorough peak fit analysis of the collected Raman spectra (see an example in [Figure 6B](#)), we find that the main component of this vibrational mode varies slightly with composition and confinement but remains within the range declared above, [Figure 6C](#). The frequency analysis of this vibrational mode indicates that the TFSI anion experiences similar interactions with its surroundings, with little dependence on the salt concentration or the surrounding polymeric network.

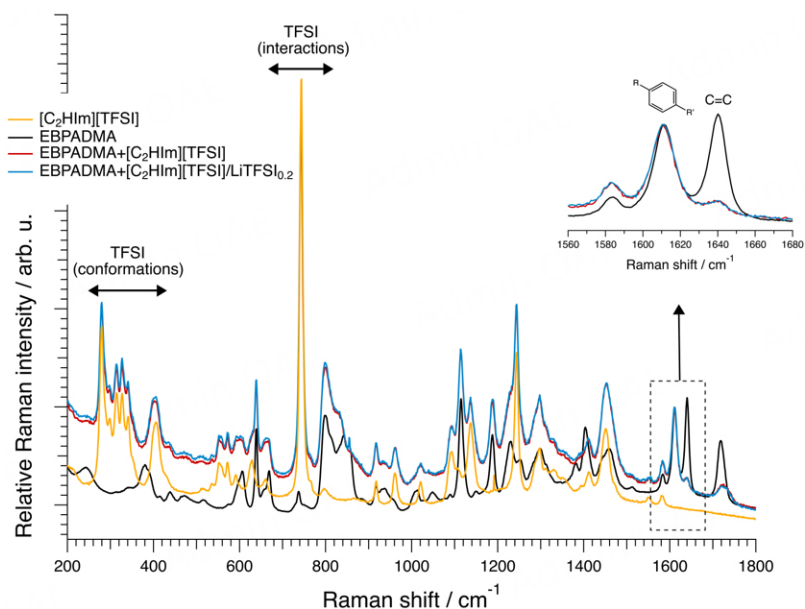


Figure 5. Selection of Raman spectra collected at room temperature for the neat protic ionic liquid ($[C_2HIm][TFSI]$), the neat monomer (EBPADMA), the cured monomer including the protic ionic liquid (EBPADMA + $[C_2HIm][TFSI]$) and the cured monomer including the protic ionic liquid mixed with LiTFSI at 0.2 m (EBPADMA + $[C_2HIm][TFSI]/LiTFSI_{0.2}$). The inset shows the vibrational modes used to estimate the degree of polymerization.

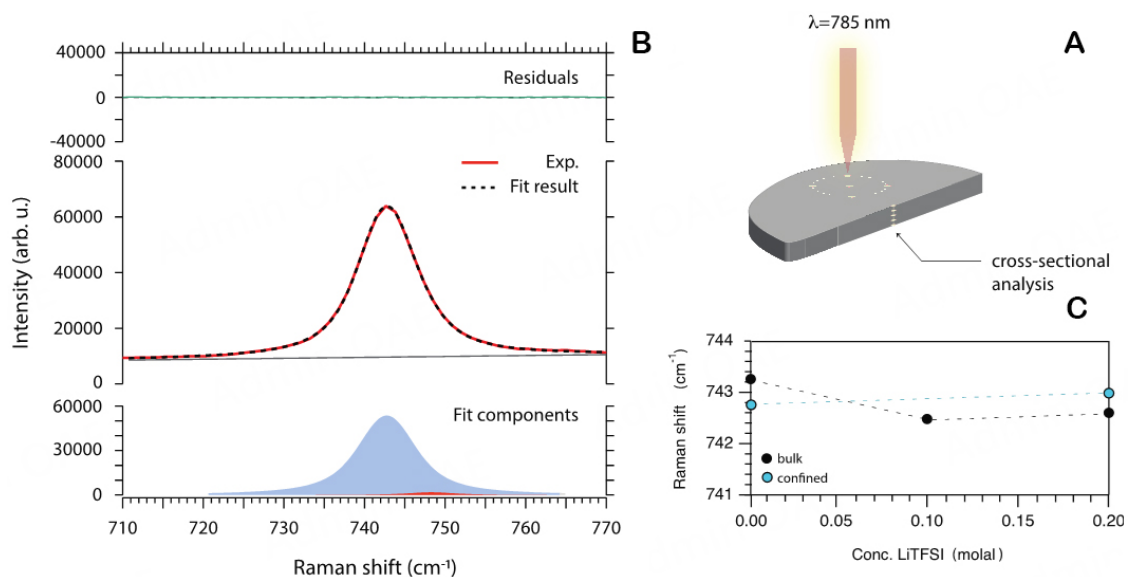


Figure 6. (A) Schematic for the collection of Raman spectra on selected spots across the material. (B) Example of peak fit analysis of a Raman spectrum. (C) Raman shifts of the interaction sensitive mode at 742 cm^{-1} (assigned to the expansion-contraction mode of the whole TFSI anion) as a function of composition for the bulk and for the confined liquid.

Ionic conductivity and mechanical stability

Quantitative insight into the impact of incorporating the liquid phase inside the polymer matrix on the ion conduction and mechanical properties can be obtained by means of dielectric spectroscopy and rheological measurements, respectively. Figure 7 shows the frequency dependence of the real part of the complex conductivity function, $\sigma^*(\omega)$, for the undoped [Figure 7A] and the LiTFSI-doped [Figure 7B] solid

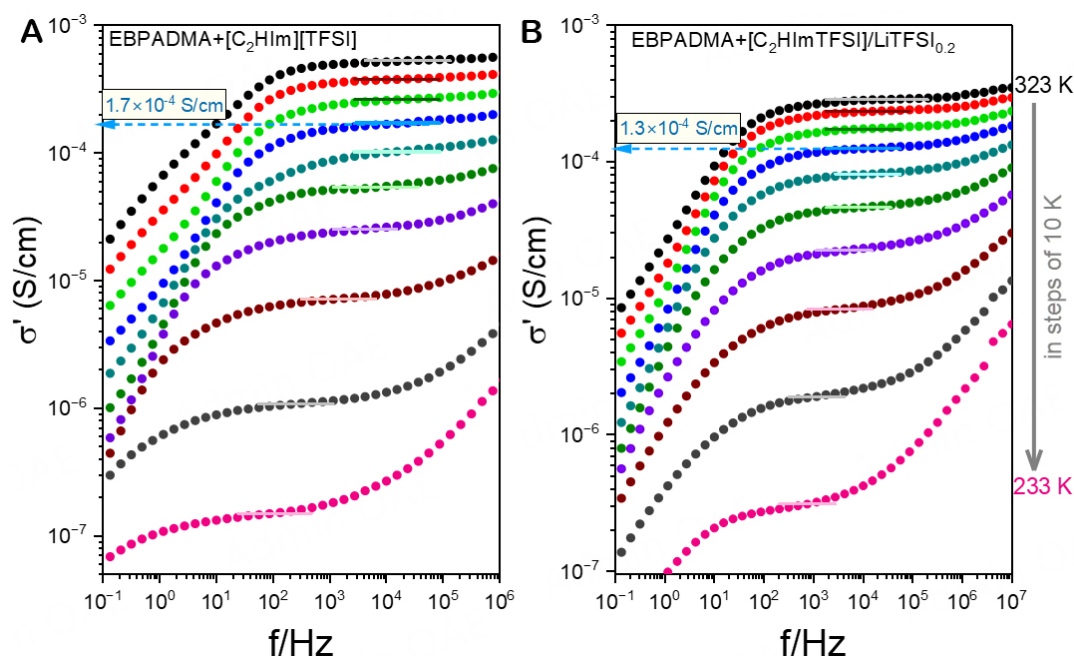


Figure 7. Frequency-dependence of the real part of the complex conductivity for (A) BPAEDMA+[C₂HIm][TFSI] and (B) BPAEDMA+[C₂HIm][TFSI]/LiTFSI_{0.2} at some selected temperatures, in steps of 10 K. The solid lines are linear fits used for determining the dc-conductivity.

electrolytes at selected temperatures. A comparison of conductivity spectra collected for EBPADMA + [C₂HIm][TFSI]/LiTFSI_{0.2} and its respective bulk liquid phase is given in the Supporting Information file as [Supplementary Figure 8](#).

At intermediate frequencies, the $\sigma'(\omega)$ curves exhibit a plateau associated with the dc-conductivity, which separates the high-frequency regime associated with ac-conductivity from the low-frequency dispersion associated with electrode polarization. Additionally, the dc-conductivity could also be extracted from the Nyquist plot, as shown in [Supplementary Figure 9](#). The extracted dc-conductivity values of the methacrylate-based solid electrolytes are presented as a function of inverse temperature in [Figure 8A](#). The ionic conductivity of the bulk liquid phase and the calorimetric T_g s are also included in this figure.

As illustrated in [Figure 8](#), the solid electrolytes exhibit about one order of magnitude lower conductivity than the corresponding bulk liquid phase. This is partly due to the fact that only 50% of the solid polymer electrolyte consists of the liquid electrolyte but mostly due to the morphology, which implies that the liquid phase encounters dead ends or narrow regions of pathways that limit or slow down the long-range translational ion diffusion between the two electrodes. After doping with LiTFSI at a concentration of 0.2 m, the conductivity slightly decreases (likely due to increased viscosity) and achieves a value of $\sigma_{dc} = 0.13$ mS/cm at 293 K. It should be mentioned that the measured total ionic conductivity comes from the transport of three mobile ionic species (Im⁺, TFSI⁻, and Li⁺), with individual contributions that can only be estimated from diffusion-NMR experiments. Notably, this NMR-based study would support the data of this work by quantifying the real mobility of each ion. From the latter, important quantities such as the real Li⁺ conductivity and the Li⁺ transference number could then be calculated. Unfortunately, such experiments require great effort and will be performed in a future study since they are not in the scope of this work. It should also be mentioned that the measured conductivities are comparable to those found in porous solid electrolytes bearing a liquid phase of the aprotic ionic liquid [C₂C₁Im][TFSI]^[22] or [C₄C₁Im][TFSI]^[25] doped

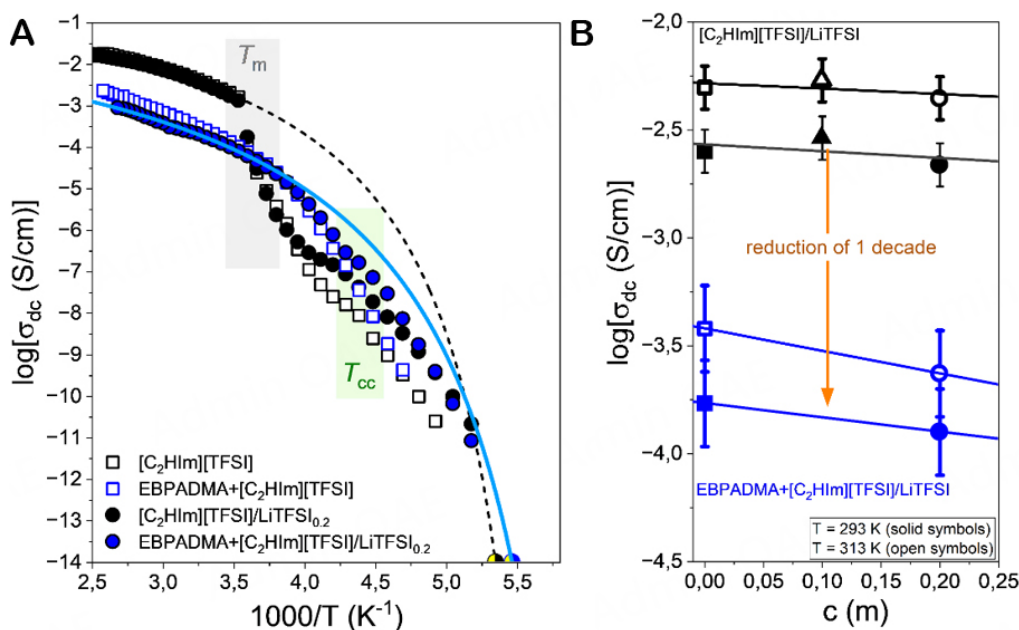


Figure 8. (A) Temperature-dependence of the ionic conductivity for the studied electrolytes; EBPADMA + $[\text{HC}_2\text{Im}][\text{TFSI}]$ (open blue symbols) and EBPADMA + $[\text{C}_2\text{HIm}][\text{TFSI}]/\text{LiTFSI}_{0.2}$ (solid blue symbols) in comparison with their respective bulk liquid electrolytes; $[\text{C}_2\text{HIm}][\text{TFSI}]$ (open black symbols) and $[\text{C}_2\text{HIm}][\text{TFSI}]/\text{LiTFSI}_{0.2}$ (filled black symbols), upon heating. The solid and dashed lines represent fits to Eq. 2 for the solid electrolyte and its corresponding bulk liquid electrolyte doped with LiTFSI at a Li-salt concentration of 0.2 m. The shadowed green and grey areas indicate the cold-crystallization and the melting, respectively. (B) Comparison of the ionic conductivity for the bulk (black symbols) and the confined (blue symbol) liquid phases at two temperatures: $T = 293 \text{ K}$ (filled symbols) and $T = 313 \text{ K}$ (open symbols).

with LiTFSI at a Li-salt concentration of 1M, as shown in [Supplementary Figure 10](#). Specifically, the temperature dependence of the dc-conductivity exhibits some discontinuity in the temperature range of the weak first order transitions (cold-crystallization/melting). These discontinuities in σ_{dc} are distinctly weaker compared to the bulk liquid phase, reflecting the lower degree of crystallinity upon confinement, in agreement with the results from DSC [Figure 4D]. The behavior of the conductivity data above the T_m holds significant importance, which can be well described by the Vogel-Fulcher-Tammann (VFT) equation written as:

$$\sigma_{dc}(T) = \sigma_0^\# \exp\left(-\frac{B}{T-T_0}\right) \tag{2}$$

where $\sigma_0^\#$ is the dc-conductivity in the limit of very high temperatures, B is a parameter related to the activation energy, and T_0 is the “ideal” T_g , which differs from the calorimetric T_g by typically $\sim 40\text{-}50 \text{ K}$. In the fitting procedure, the calorimetric T_g value was also included. The ionic conductivity at T_g was calculated by employing the Nernst-Einstein equation as $\sigma_{dc}(T_g) = \frac{ne^2}{k_B T} \frac{d_{11}^2}{6\tau}$, where $n = \frac{\rho N_A}{M_w}$ (ρ is the density, and M_w is the molar mass of the repeat unit) is the number density of the mobile anions, $d_{11}/2$ is the charge-alternation distance between two adjacent ions of opposite charge^[28], τ ($\approx 100 \text{ s}$) is the characteristic structural relaxation time at T_g , and k_B is the Boltzmann constant. The VFT parameters found from fitting the data of [Figure 8](#) and [Supplementary Figure 11](#) of the SBEs and their bulk liquid phases are summarized in [Table 1](#).

Table 1. VFT parameters obtained from fitting conductivity data

Sample	Log [σ_0 (S/cm)]	B (K)	T_0 (K)	R^2
[C ₂ HIm][TFSI]	0.58 ± 0.03	590 ± 10	166.0 ± 0.5	0.99998
[C ₂ HIm][TFSI]/LiTFSI _{0.2}	0.67 ± 0.02	570 ± 10	166.6 ± 0.3	0.99996
EBPADMA + [C ₂ HIm][TFSI]	0.93 ± 0.01	944 ± 7	148.6 ± 0.2	0.99996
EBPADMA + [C ₂ HIm][TFSI]/LiTFSI _{0.2}	1.61 ± 0.05	720 ± 20	157.8 ± 0.6	0.99987

As mentioned in the introduction, achieving mechanically robust solid electrolytes is often limited by the competing need for efficient ion transport. The mechanical properties of the investigated thermally cured methacrylate-based electrolytes were, hence, also analyzed by carrying out rheological measurements in an oscillatory mode as a function of temperature under isochronal conditions ($\omega = 10$ rad/s) and as a function of frequency under isothermal conditions, that is at 318 K ($T < T_g^{\text{EBPADMA}}$) and at 373 K ($T > T_g^{\text{EBPADMA}}$). The results from these measurements are provided in [Figure 9](#).

As shown in [Figure 9A](#), the temperature dependence of the shear storage modulus exhibits a weak and broad step change at around 360 K, associated with the T_g^{EBPADMA} . The broadness of this feature reflects the different degrees of cross-linking in the polymer matrix. It is also clear that the temperature dependence of the dc-conductivity remains unaffected by the T_g of the hard polymer phase, reflecting a strong segregation between the two phases. Quantitative insights into mechanical properties can be obtained by performing isothermal frequency sweeps into the linear viscoelastic regime, as shown in [Figure 9B](#). At $T = 318$ K ($T < T_g^{\text{EBPADMA}}$), the storage moduli, G' , exceeds the loss moduli, G'' ($G' \gg G''$), by about one order of magnitude, and they are almost independent of the angular frequency ($G' \sim \omega^0$, $G'' \sim \omega^0$). At the same temperature, the bulk ion-conducting phase is in the liquid state ($G' \sim \omega^2$ and $G'' \sim \omega^1$). To summarize, at $T = 318$ K, we report a combination of elastic behavior with a shear modulus of 100 MPa and a conductivity of 0.26 mS/cm. At $T = 373$ K, the shear modulus remains as high as 10 MPa, exhibiting an elastic behavior (cross-linked polymer matrix), and simultaneously, the ionic conductivity achieves a value of 0.9 mS/cm. Hence, the investigated SBEs exhibit a good combination of ionic conductivity and mechanical stiffness; this can also be judged from [Figure 10](#), which compares our results with those of other works available in the literature.

The multifunctionality plot, as shown in [Figure 10](#), evidences the trade-off between ion conduction and mechanical properties. It is worth mentioning that the room temperature ionic conductivity of the cross-linked structural electrolytes is more than two orders of magnitude higher than that found in different types of solid electrolytes previously studied (e.g., polymerized ionic liquids and block copolymer electrolytes based on the PEO conductive phase)^[64-66], despite equivalent shear modulus (~ 100 MPa). However, the ionic conductivity of the investigated structural electrolytes remains one order of magnitude lower than the ionic conductivity of the bulk liquid phase and the target set for electrolytes intended to be used in structural batteries. To further increase the ionic conductivity of these materials, the effect of confinement and pore connectivity on the mobility of the liquid phase has to be better understood.

Relaxation dynamics - dynamic heterogeneity in the vicinity of T_g

Precise information about the ion dynamics and the coupled structural relaxation over a broad range of frequencies and temperatures can be obtained by combining dielectric spectroscopy measurements with TM-DSC^[67-70]. The latter experimental technique provides quantitative insights into structural relaxation in ionic systems, for which strong electrode polarization effects prevent a dielectric identification of the structural α -process. Together, these two techniques enable us to understand the influence of confinement and morphology on the ion conduction process.

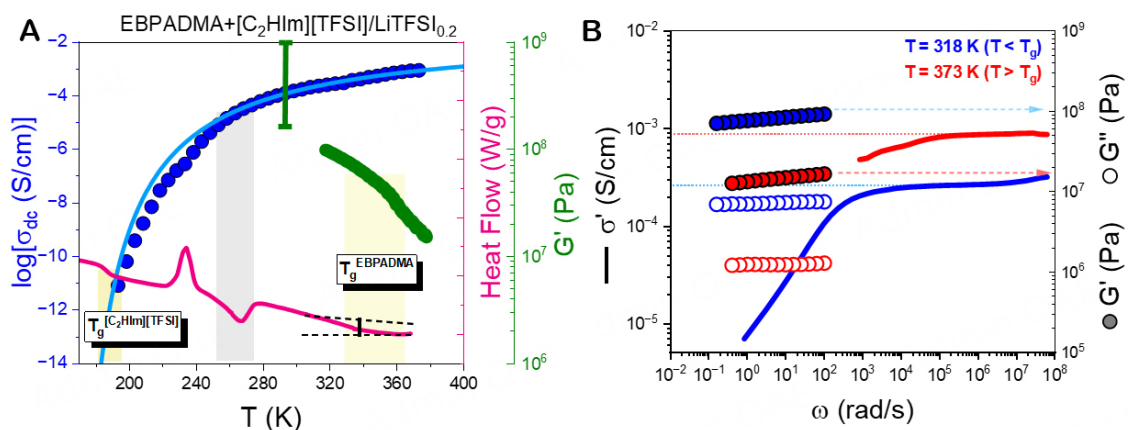


Figure 9. (A) Temperature dependence of the dc-conductivity (blue symbols), heat flow (rate = 10 K/min, magenta line), and mechanical storage moduli (green symbols, rate = 5 K/min, $\omega = 10$ rad/s). The scale bar denotes the range of elastic storage moduli reported in the literature for SBEs with similar polymer matrices^[13-25]. (B) Real part of the complex conductivity (solid lines) compared with the storage (filled circles) and loss (open circles) moduli at $T = 318$ K ($T < T_g$) (blue symbols) and $T = 373$ K ($T > T_g$) (red symbols).

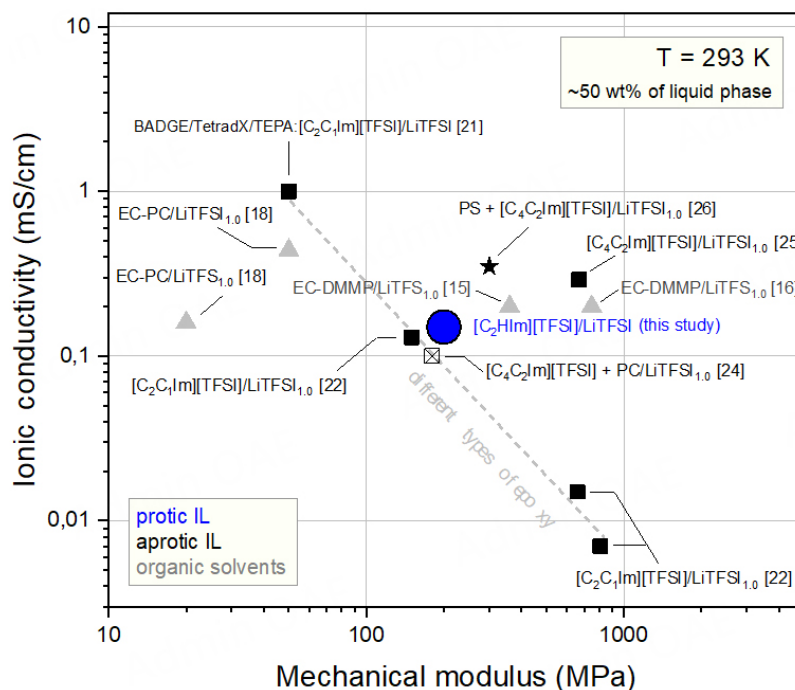


Figure 10. Multifunctionality plot that compares the properties of the structural battery electrolyte investigated in this study (blue solid circle) with those of other equivalent electrolytes reported in the literature, all being based on bisphenol A epoxy resin but different liquid phases of ionic liquids^[21,22,24,25] or organic solvents^[15,16,18]. A solid electrolyte based on a cross-linked polystyrene (PS) polymer matrix and an ion-conducting phase consisting of a mixture of poly(ethylene oxide) (PEO) and an aprotic ionic liquid is also included in this comparative plot^[26].

In ion-conducting systems, the imaginary part of the complex electric modulus, M'' , emphasizes the contributions of translational ionic motions (ranging from long to short distances) that are associated with the conductivity process. From the peak frequency of M'' , the characteristic relaxation time of the ionic motion can be extracted by employing the empirical function suggested by Kohlrausch, Williams, and Watts, which is expressed as:

$$\phi(t) = \exp\left[-\left(\frac{t}{\tau_\sigma}\right)^{\beta_{\text{KWW}}}\right] \quad (3)$$

where t is the time, τ_σ is the characteristic conductivity relaxation time, and β_{KWW} ($0 < \beta_{\text{KWW}} < 1$) is the shape parameter related to the broadening of the relaxation peak. Lower values of β_{KWW} denote broader and more asymmetric peaks. As proposed earlier by Bergman^[71], the M'' peak can be directly fitted in the frequency domain by the following function:

$$M'' = \sum_n \frac{M''_{\text{max},n}}{(1-\beta_n) + (\beta_n/(1+\beta_n))[\beta_n(\omega_{\text{max},n}/\omega) + (\omega/\omega_{\text{max},n})^{\beta_n}]} \quad (4)$$

where M''_{max} is the peak value of M'' , and ω_{max} is the corresponding frequency. Some representative fitting curves are shown in [Supplementary Figure 12](#) for the case of the σ -process. The inclusion of the bulk liquid phase into the polymer structure significantly affects the relaxation dynamics, as shown in [Figure 11A](#), which compares the horizontally shifted electric modulus curves by employing the principle of time-temperature-superposition (tT s). The obtained shape parameter and relaxation map for the investigated solid and liquid electrolytes are shown in [Figure 11B](#) and [C](#).

From [Figure 11](#), it becomes clear that the σ -process speeds up under confinement as a result of the lower T_g , in accordance with the results from TM-DSC data. This finding supports the hypothesis of weak interfacial interactions between the two phases (solid and liquid) and a clear impact of the geometrical confinement. The speeding-up in dynamics is less evident in the confined liquid phase doped with LiTFSI, despite the fact that the calorimetric T_g reduces by about 4 K [[Supplementary Figure 13](#)]. This indicates that the structural α -relaxation and the σ -process are not coupled in the same way in the systems with and without LiTFSI. Moreover, we can observe a clear reduction in the intensity of the M'' peak and a broadening of relaxation times upon confinement, in accordance with previous studies^[43-49,51,53-55]. Specifically, the mean value of the shape parameter β_{KWW} decreases from 0.55 (0.65) to 0.4 (0.4) in going from the respective bulk liquid phases to the neat (doped with LiTFSI) solid electrolytes. A plausible reason for this is that the dynamics become more heterogeneous upon confinement, with slower dynamics at the polymer interface than in the central region of the pores^[43,45,54,55].

The extracted relaxation times of the σ -process can be discussed together with the TM-DSC data with respect to the relaxation map of [Figure 11C](#). Evidently, the σ -process is coupled to the structural α -process. The σ -process can be well described by the VFT equation^[72,73]:

$$\tau_{\text{max}} = \tau_0^\# \exp\left(\frac{B}{T-T_0}\right) \quad (5)$$

In this equation, $\tau_0^\#$ is the relaxation time at very high temperatures, B is the pseudo-activation parameter, and T_0 is the "ideal" glass temperature located below the conventional T_g . Extrapolation of the fit to a relaxation time of 100 s gives the dielectric liquid-to-glass transition temperature. The VFT parameters and the dielectric T_g , along with the TM-DSC data, are summarized in [Table 2](#).

The steepness index or the fragility parameter, m , provides information about the temperature dependence of τ_σ and the coupled structural relaxation and can be extracted from the slope in the "fragility" plot of $\log(\tau)$ vs. T_g/T . It can also be calculated by employing the VFT parameters as $m^* = BT_g/[2.303(T_g-T_0)^2]$ ^[74]. The values of m calculated in this way are reported in [Table 2](#). We find that fragility slightly increases in the

Table 2. VFT parameters for the σ -process, glass transition temperature, and fragility parameter for the investigated electrolytes

Sample	Dielectric spectroscopy					TMDSC				
	$-\log(\sigma_0/s)^a$ ($-\tau_0/s$) ^a	B (K)	T_0 (K)	T_g (K) ^b	R^2	m^*	N_a^D	T_g (K)	ζ_a (nm)	
[C ₂ HIm][TFSI]	-12	1770 ± 10	128.1 ± 0.4	183.1 ± 0.4	0.9997	44	110	184	2.6	
[C ₂ HIm][TFSI]/LiTFSI _{0.2}	-12	1550 ± 50	137 ± 2	185.0 ± 2.0	0.9784	50	115	187	2.7	
EBPADMA + [C ₂ HIm][TFSI]	-12	1630 ± 20	128.7 ± 0.7	179.0 ± 0.7	0.9992	47	7	180	1.0	
EBPADMA + [C ₂ HIm][TFSI]/LiTFSI _{0.2}	-12	1440 ± 30	138 ± 1	183.0 ± 1.0	0.9976	57	8	183	1.2	

^aHeld fixed; ^b $\tau = 100$ s, from the VFT fit of both the dielectric and TM-DSC data.

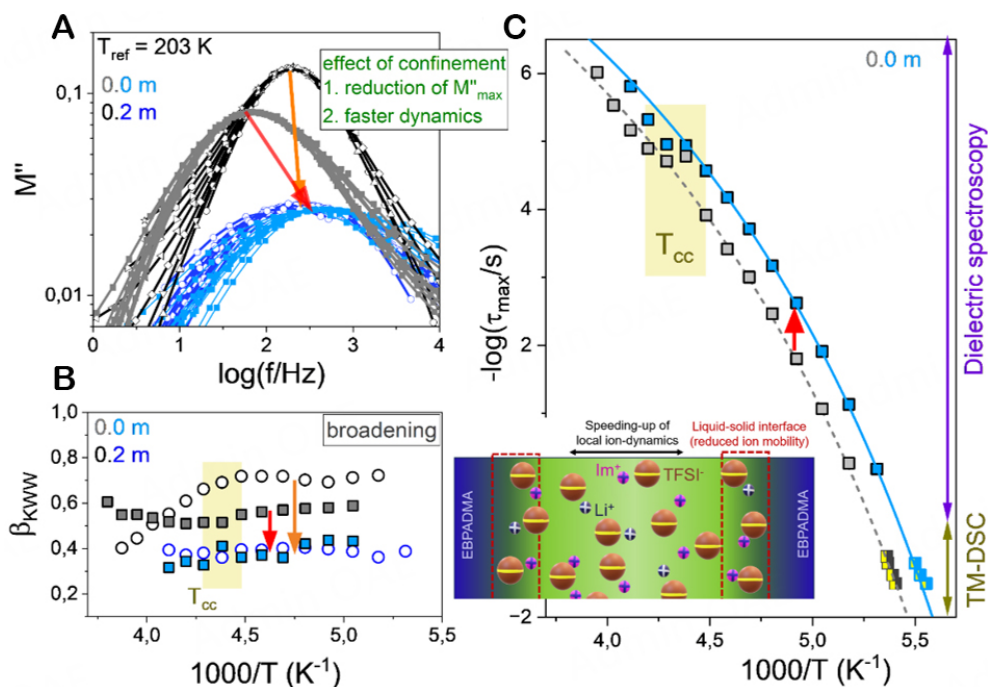


Figure 11. (A) Complex electric modulus (M'') curves shifted to the peak maximum of the σ -process by employing the tT s principle, at a reference temperature of 203 K, for the [C₂HIm][TFSI] (grey symbols), C₂HIm][TFSI]/LiTFSI_{0.2} (black symbols), EBPADMA + [C₂HIm][TFSI] (cyan symbols) and EBPADMA + [C₂HIm][TFSI]/LiTFSI_{0.2} (blue symbols). (B) The shape parameter, β_{KWW} , of the σ -process, as a function of inverse temperature. (C) Relaxation map depicting the σ -process and the relaxation times of the structural α -process extracted from TM-DSC (circles in yellow) for the undoped electrolytes. The solid and dashed lines represent fits by the VFT equation (Eq. 5) to the temperature dependence of the σ -relaxation of the solid electrolytes and their respective bulk protic ionic liquids. The colored area indicates the cold-crystallization region. (Inset) An illustration of the gradient of viscosity that most likely takes place between the liquid and solid phases. The green (blue) color indicates the region with the lower (higher) effective medium's viscosity. The interfacial region between the two segregated phases is indicated by dashed lines.

confined liquid phase, a similar trend to that found in, e.g., hydrogen-bonded liquids based on propylene glycol mono methyl ether (PGME) confined in two-dimensional vermiculite clay^[46]. This suggests that the interaction between the molecules (network character) decreases in confinement, possibly due to an increase of the free volume and/or geometrical restrictions of orientational ordering.

Precise information about the heterogeneous dynamics and the dynamic nature of T_g can be obtained by taking into account the idea of cooperatively rearranging regions (CRR) introduced by Adam and Gibbs^[75]. A CRR is defined as the smallest volume element that can rearrange to a new configuration independently

of its environment. Based on the fluctuation theorem, Donth proposed a model for describing this volume as^[76]:

$$V_a(T_g) = \frac{k_B T_g^2 \Delta(1/C_p)}{\rho(\delta T)^2} \quad (6)$$

where k_B is the Boltzmann constant, and $\Delta(1/C_p) = 1/C_p^{\text{glass}} - 1/C_p^{\text{liquid}}$ calculated at T_g and $\delta T (= \Delta T/2.5)$ is the mean temperature fluctuation of a CRR. According to Donth's prediction, considering a sphere with volume V_a , the correlation length of T_g can be calculated as $\xi_a = (3V_a/4\pi)^{1/3}$ and the number of correlated molecules close to T_g as $N_a = \frac{V_a \rho N_A}{M}$. Hence, by employing Eq. 6, the N_a and ξ_a are given by^[76]:

$$N_a = \frac{V_a \rho N_A}{M} = \frac{RT_g^2 \Delta(1/C_p)}{(\delta T)^2 M} \quad (7)$$

$$\xi_a = \left(\frac{3V_a}{4\pi}\right)^{1/3} = \left(\frac{3k_B T_g^2 \Delta(1/C_p)}{4\pi \rho (\delta T)^2}\right)^{1/3} \quad (8)$$

where N_A is the Avogadro number, $R (= k_B \cdot N_A)$ is the gas constant, M is the molar mass of the repeating unit, and ρ is the density. The parameter values employed in the Donth model are taken from the TM-DSC data presented in Figure 4B. The values of N_a and ξ_a are also provided in Table 2. However, it should be noted that the calculation of N_a requires knowledge of the density of the confined liquid phase, a value that is difficult to estimate. Hence, we will emphasize our discussion only on the calculated length scale of T_g . The length scale of T_g decreases from 2.7 nm to 1.2 nm upon confinement for the structural electrolyte doped with LiTFSI, implying smaller regions of cooperativity in the confined liquid phase. This finding further supports the hypothesis of a lower liquid density in the pores, once again reflecting the impact of geometrical confinement.

This is the first time that the impact of confining a PIL into a polymer matrix on relaxation dynamics and associated local ionic mobility has been investigated by employing a combination of dielectric spectroscopy and TM-DSC. These techniques are well-known in the research field of polymer science (covering more than eight decades of frequencies) but have not been used in the research field of Structural Batteries to study the local dynamics. In contrast, we provide the first insights into how the local relaxation dynamics and the associated local ionic mobility are affected by the confinement in the porous polymer network. We demonstrate that the dynamics are enhanced by the confinement despite the relatively strong reduction of the macroscopic ionic conductivity. This emphasizes the importance of synthesizing a polymer network with percolating pores (i.e., minimizing the number of dead-ends) for reaching the desired ionic conductivity in the design of novel Structural Electrolytes.

CONCLUSIONS

In this work, we investigate the ion coordination, the thermodynamic properties, the ionic conductivity, the morphological properties, and the mechanical stability in nanophase-separated SBEs, composed of methacrylate-based polymer (EBPADMA) combined with the imidazolium PIL [C₂HIm][TFSI] doped with LiTFSI. To the best of our knowledge, this is the first study of a PIL incorporated into a methacrylate-based polymer matrix. We report that the confinement of the liquid phase significantly reduces the degree of crystallinity, yielding almost amorphous electrolytes. Moreover, we report a speeding-up of ion dynamics that are coupled to the structural relaxation, hence a reduction of T_g by about 4 K. The latter implies that the interfacial interactions are weak and that the geometrical confinement effect is the main factor that dictates

the local ion dynamics and the coupled structural relaxation. Furthermore, the Raman spectroscopy results show that the TFSI anion establishes spectroscopically weak interactions with its surroundings, even upon confinement. However, despite the speeding-up of the molecular motions in confinement (at least at temperatures close to T_g), the dc-conductivity decreases upon confinement to $\sigma_{dc} \sim 0.13$ mS/cm at $T = 293$ K, which is one decade lower than the value of the bulk liquid phase. The reason for this is likely the presence of some non-percolating pores, which reduces the long-range translation of the ions. Thus, to reach the desired dc-conductivity of 1 mS/cm for these types of SBEs, it will be essential to improve the connectivity and network character of the pores. Moreover, since three mobile ions (Im^+ , TFSI $^-$, and Li^+) contribute to the measured total ionic conductivity, the Li^+ transference number will have to be measured by, e.g., diffusion-NMR. On the other hand, we report that the solid electrolytes exhibit the required mechanical stability needed to carry the mechanical loads between the carbon fibers in structural batteries. Overall, we conclude that microphase-separated copolymer electrolytes consisting of a methacrylate-based polymer matrix and protic imidazolium ionic liquids doped with LiTFSI are promising for use in future mass-less structural batteries.

SUPPORTING INFORMATION

Additional TGA, SEM images, TM-DSC, Raman spectroscopy, and dielectric spectroscopy data.

DECLARATIONS

Acknowledgments

This work was financially supported by a grant from the Area of Advance *Materials Science* at Chalmers University of Technology. The authors also thank Dr. Andreas Schaefer for help in the nitrogen sorption measurements and Dr. Mei Qun Seah for help with the SEM images.

Authors' contributions

DSC-TMDSC, dielectric and rheological experiments, data analysis, writing most of the first draft of the manuscript: Pipertzis A

Synthesis of SBEs and their respective bulk liquid phases, TGA, textural and morphological analysis (nitrogen sorption and SEM), Raman experiments and Raman data analysis, writing parts of the first draft of the manuscript: Abdou N

Mixing of liquid electrolytes, interpretation of results, contributing to the writing of the manuscript: Xu J

Conceptualization, interpretation of results, contributing to the writing of the manuscript: Asp LE

Conceptualization, data interpretation, contributing to the writing of the manuscript: Martinelli A

Conceptualization, data interpretation, contributing to the writing of the manuscript: Swenson J

Availability of data and materials

The data is available on request.

Financial support and sponsorship

This work was financially supported by a grant from the Area of Advance Materials Science at Chalmers University of Technology.

Conflicts of Interest

All authors declared that there are no conflicts of interest.

Ethical approval and consent to participate

Not applicable.

Consent for publication

Not applicable.

Copyright

© The Author(s) 2023.

REFERENCES

1. Goodenough JB. Electrochemical energy storage in a sustainable modern society. *Energy Environ Sci* 2014;7:14-8. DOI
2. Tarascon JM, Armand M. Issues and challenges facing rechargeable lithium batteries. *Nature* 2001;414:359-67. DOI PubMed
3. Asp LE, Johansson M, Lindbergh G, Xu J, Zenkert D. Structural battery composites: a review. *Funct Compos Struct* 2019;1:042001. DOI
4. Asp LE, Bouton K, Carlstedt D, et al. A structural battery and its multifunctional performance. *Adv Energy Sustain Res* 2021;2:2000093. DOI
5. Lim GJH, Chan KK, Sutrisnoh NAA, Srinivasan M. Design of structural batteries: carbon fibers and alternative form factors. *Mater Today Sustain* 2022;20:100252. DOI
6. Greenhalgh ES, Nguyen S, Valkova M, Shirshova N, Shaffer MSP, Kucernak ARJ. A critical review of structural supercapacitors and outlook on future research challenges. *Compos Sci Technol* 2023;235:109968. DOI
7. Jin T, Singer G, Liang K, Yang Y. Structural batteries: advances, challenges and perspectives. *Mater Today* 2023;62:151-67. DOI
8. Danzi F, Salgado RM, Oliveira JE, Arteiro A, Camanho PP, Braga MH. Structural batteries: a review. *Molecules* 2021;26:2203. DOI PubMed PMC
9. Carlstedt D, Asp LE. Performance analysis framework for structural battery composites in electric vehicles. *Compos B Eng* 2020;186:107822. DOI
10. Ishfaq A, Nguyen SN, Greenhalgh ES, et al. Multifunctional design, feasibility and requirements for structural power composites in future electric air taxis. *J Compos Mater* 2023;57:817-27. DOI
11. Kühnelt H, Beutl A, Mastropiero F, et al. Structural batteries for aeronautic applications - state of the art, research gaps and technology development needs. *Aerospace* 2022;9:7. DOI
12. Thomas JP, Qidwai SM, Pogue WR III, Pham GT. Multifunctional structure-battery composites for marine systems. *J Compos Mater* 2013;47:5-26. DOI
13. Tan MY, Safanama D, Goh SS, et al. Concepts and emerging trends for structural battery electrolytes. *Chem Asian J* 2022;17:e202200784. DOI
14. Snyder JF, Carter RH, Wetzel ED. Electrochemical and mechanical behavior in mechanically robust solid polymer electrolytes for use in multifunctional structural batteries. *Chem Mater* 2007;19:3793-801. DOI
15. Ihrner N, Johannisson W, Sieland F, Zenkert D, Johansson M. Structural lithium ion battery electrolytes via reaction induced phase-separation. *J Mater Chem A* 2017;5:25652-9. DOI
16. Schneider LM, Ihrner N, Zenkert D, Johansson M. Bicontinuous electrolytes via thermally initiated polymerization for structural lithium ion batteries. *ACS Appl Energy Mater* 2019;2:4362-9. DOI
17. Cattaruzza M, Fang Y, Furó I, Lindbergh G, Liu F, Johansson M. Hybrid polymer-liquid lithium ion electrolytes: effect of porosity on the ionic and molecular mobility. *J Mater Chem A* 2023;11:7006-15. DOI
18. Fu Y, Chen Y, Yu X, Zhou L. Fiber metal laminated structural batteries with multifunctional solid polymer electrolytes. *Compos Sci Technol* 2022;230:109731. DOI
19. Choi J, Zabihi O, Varley R, Zhang J, Fox BL, Naebe M. Multiple hydrogen bond channel structural electrolyte for an enhanced carbon fiber composite battery. *ACS Appl Energy Mater* 2022;5:2054-66. DOI
20. Choi J, Zabihi O, Varley RJ, Fox B, Naebe M. High performance carbon fiber structural batteries using cellulose nanocrystal reinforced polymer electrolyte. *ACS Appl Mater Interfaces* 2022;14:45320-32. DOI PubMed
21. Matsumoto K, Endo T. Confinement of ionic liquid by networked polymers based on multifunctional epoxy resins. *Macromolecules* 2008;41:6981-6. DOI
22. Shirshova N, Bismarck A, Carreyette S, et al. Structural supercapacitor electrolytes based on bicontinuous ionic liquid-epoxy resin systems. *J Mater Chem A* 2013;1:15300-9. DOI
23. Shirshova N, Bismarck A, Greenhalgh ES, et al. Composition as a means to control morphology and properties of epoxy based dual-phase structural electrolytes. *J Phys Chem C* 2014;118:28377-87. DOI
24. Yu Y, Zhang B, Feng M, et al. Multifunctional structural lithium ion batteries based on carbon fiber reinforced plastic composites. *Compos Sci Technol* 2017;147:62-70. DOI
25. Kwon SJ, Kim T, Jung BM, Lee SB, Choi UH. Multifunctional epoxy-based solid polymer electrolytes for solid-state supercapacitors. *ACS Appl Mater Interfaces* 2018;10:35108-17. DOI
26. Schulze MW, McIntosh LD, Hillmyer MA, Lodge TP. High-modulus, high-conductivity nanostructured polymer electrolyte membranes via polymerization-induced phase separation. *Nano Lett* 2014;14:122-6. DOI PubMed
27. Armand M, Endres F, MacFarlane DR, Ohno H, Scrosati B. Ionic-liquid materials for the electrochemical challenges of the future. *Nat*

- Mater* 2009;8:621-9. [DOI](#) [PubMed](#)
28. Abdurrokhman I, Elamin K, Danyliv O, Hasani M, Swenson J, Martinelli A. Protic ionic liquids based on the alkyl-imidazolium cation: effect of the alkyl chain length on structure and dynamics. *J Phys Chem B* 2019;123:4044-54. [DOI](#) [PubMed](#)
 29. Martinelli A, Matic A, Jacobsson P, Börjesson L, Fernicola A, Scrosati B. Phase behavior and ionic conductivity in lithium bis(trifluoromethanesulfonyl)imide-doped ionic liquids of the pyrrolidinium cation and bis(trifluoromethanesulfonyl)imide anion. *J Phys Chem B* 2009;113:11247-51. [DOI](#) [PubMed](#)
 30. Pitawala J, Kim JK, Jacobsson P, Koch V, Croce F, Matic A. Phase behaviour, transport properties, and interactions in Li-salt doped ionic liquids. *Faraday Discuss* 2012;154:71-80; discussion 81-96, 465-71. [DOI](#) [PubMed](#)
 31. Martinelli A, Matic A, Johansson P, et al. Conformational evolution of TFSI in protic and aprotic ionic liquids. *J Raman Spectrosc* 2011;42:522-8. [DOI](#)
 32. Nasrabad AT, Ganesan V. Structure and transport properties of lithium-doped aprotic and protic ionic liquid electrolytes: insights from molecular dynamics simulations. *J Phys Chem B* 2019;123:5588-600. [DOI](#) [PubMed](#)
 33. Jafta CJ, Bridges C, Haupt L, et al. Ion dynamics in ionic-liquid-based li-ion electrolytes investigated by neutron scattering and dielectric spectroscopy. *ChemSusChem* 2018;11:3512-23. [DOI](#)
 34. Singh MP, Singh RK, Chandra S. Ionic liquids confined in porous matrices: physicochemical properties and applications. *Prog Mater Sci* 2014;64:73-120. [DOI](#)
 35. Abdou N, Alonso B, Brun N, et al. Ionic guest in ionic host: ionosilica ionogel composites via ionic liquid confinement in ionosilica supports. *Mater Chem Front* 2022;6:939-47. [DOI](#)
 36. Abdou N, Alonso B, Brun N, et al. Confinement effects on the ionic liquid dynamics in ionosilica ionogels: impact of the ionosilica nature and the host/guest ratio. *J Phys Chem C* 2022;126:20937-45. [DOI](#)
 37. Martinelli A, Nordstierna L. An investigation of the sol-gel process in ionic liquid-silica gels by time resolved Raman and 1H NMR spectroscopy. *Phys Chem Chem Phys* 2012;14:13216-23. [DOI](#) [PubMed](#)
 38. Martinelli A. Conformational changes and phase behaviour in the protic ionic liquid 1-ethylimidazolium bis(trifluoromethylsulfonyl)imide in the bulk and nano-confined state. *Eur J Inorg Chem* 2015;2015:1300-8. [DOI](#)
 39. Nayeri M, Aronson MT, Bernin D, Chmelka BF, Martinelli A. Surface effects on the structure and mobility of the ionic liquid C6C1ImTFSI in silica gels. *Soft Matter* 2014;10:5618-27. [DOI](#) [PubMed](#)
 40. Vavra S, Elamin K, Evenäs L, Martinelli A. Transport properties and local structure of an imidazole/protic ionic liquid mixture confined in the mesopores of hydrophobic silica. *J Phys Chem C* 2021;125:2607-18. [DOI](#)
 41. Morais EM, Abdurrokhman I, Martinelli A. Solvent-free synthesis of protic ionic liquids. Synthesis, characterization and computational studies of triazolium based ionic liquids. *J Mol Liq* 2022;360:119358. [DOI](#)
 42. Menne S, Pires J, Anouti M, Balducci A. Protic ionic liquids as electrolytes for lithium-ion batteries. *Electrochem Commun* 2013;31:39-41. [DOI](#)
 43. Cerveny S, Mallamace F, Swenson J, Vogel M, Xu L. Confined water as model of supercooled water. *Chem Rev* 2016;116:7608-25. [DOI](#) [PubMed](#)
 44. Swenson J, Cerveny S. Dynamics of deeply supercooled interfacial water. *J Phys Condens Matter* 2015;27:033102. [DOI](#)
 45. Swenson J, Elamin K, Jansson H, Kittaka S. Why is there no clear glass transition of confined water? *Chem Phys* 2013;424:20-5. [DOI](#)
 46. Cerveny S, Mattsson J, Swenson J, Bergman R. Relaxations of hydrogen-bonded liquids confined in two-dimensional vermiculite clay. *J Phys Chem B* 2004;108:11596-603. [DOI](#)
 47. Swenson J, Jansson H, Bergman R. Relaxation processes in supercooled confined water and implications for protein dynamics. *Phys Rev Lett* 2006;96:247802. [DOI](#) [PubMed](#)
 48. Ananiadou A, Papamokos G, Steinhart M, Floudas G. Effect of confinement on the dynamics of 1-propanol and other monohydroxy alcohols. *J Chem Phys* 2021;155:184504. [DOI](#) [PubMed](#)
 49. Tu CH, Veith L, Butt HJ, Floudas G. Ionic conductivity of a solid polymer electrolyte confined in nanopores. *Macromolecules* 2022;55:1332-41. [DOI](#)
 50. Iacob C, Sangoro JR, Kipnusu WK, Valiullin R, Kärger J, Kremer F. Enhanced charge transport in nano-confined ionic liquids. *Soft Matter* 2012;8:289-93. [DOI](#)
 51. Tu W, Chat K, Szklarz G, et al. Dynamics of pyrrolidinium-based ionic liquids under confinement. II. the effects of pore size, inner surface, and cationic alkyl chain length. *J Phys Chem C* 2020;124:5395-408. [DOI](#)
 52. Berrod Q, Ferdeghini F, Judeinstein P, et al. Enhanced ionic liquid mobility induced by confinement in 1D CNT membranes. *Nanoscale* 2016;8:7845-8. [DOI](#)
 53. Alexandris S, Papadopoulos P, Sakellariou G, Steinhart M, Butt HJ, Floudas G. Interfacial energy and glass temperature of polymers confined to nanoporous alumina. *Macromolecules* 2016;49:7400-14. [DOI](#)
 54. Alcoutlabi M, McKenna GB. Effects of confinement on material behaviour at the nanometre size scale. *J Phys Condens Matter* 2005;17:461. [DOI](#)
 55. Busselez R, Lefort R, Ji Q, Affouard F, Morineau D. Molecular dynamics simulation of nanoconfined glycerol. *Phys Chem Chem Phys* 2009;11:11127-33. [DOI](#) [PubMed](#)
 56. Brunauer S, Emmett PH, Teller E. Adsorption of gases in multimolecular layers. *J Am Chem Soc* 1938;60:309-19. [DOI](#)
 57. Barrett EP, Joyner LG, Halenda PP. The determination of pore volume and area distributions in porous substances. I. computations from nitrogen isotherms. *J Am Chem Soc* 1951;73:373-80. [DOI](#)

58. Wunderlich B, Jin Y, Boller A. Mathematical description of differential scanning calorimetry based on periodic temperature modulation. *Thermochim Acta* 1994;238:277-93. [DOI](#)
59. Simon SL. Temperature-modulated differential scanning calorimetry: theory and application. *Thermochim Acta* 2001;374:55-71. [DOI](#)
60. Shin WS, Li XF, Schwartz B, Wunder SL, Baran GR. Determination of the degree of cure of dental resins using Raman and FT-Raman spectroscopy. *Dent Mater* 1993;9:317-24. [DOI](#) [PubMed](#)
61. Gejji SP, Suresh CH, Babu K, Gadre SR. Ab initio structure and vibrational frequencies of $(CF_3SO_2)_2N^+ Li^+$ ion pairs. *J Phys Chem A* 1999;103:7474-80. [DOI](#)
62. Guyomard-Lack A, Delannoy PE, Dupré N, Cerclier CV, Humbert B, Le Bideau J. Deconstructing ionic liquids in ionogels: enhanced fragility for solid devices. *Phys Chem Chem Phys* 2014;16:23639-45. [DOI](#) [PubMed](#)
63. Aidoud D, Guy-bouyssou D, Guyomard D, Bideau JL, Lestriez B. Photo-polymerized organic host network of ionogels for lithium batteries: effects of mesh size and of ethylene oxide content. *J Electrochem Soc* 2018;165:A3179. [DOI](#)
64. Dreier P, Pipertzis A, Spyridakou M, Mathes R, Floudas G, Frey H. Introduction of trifluoromethanesulfonamide groups in poly(ethylene oxide): ionic conductivity of single-ion-conducting block copolymer electrolytes. *Macromolecules* 2022;55:1342-53. [DOI](#)
65. Pipertzis A, Kafetzi M, Giaouzi D, Pispas S, Floudas GA. Grafted copolymer electrolytes based on the poly(acrylic acid-co-oligo ethylene glycol acrylate) (P(AA-co-OEGA)) ion-conducting and mechanically robust block. *ACS Appl Polym Mater* 2022;4:7070-80. [DOI](#)
66. Pipertzis A, Papamokos G, Mühlinghaus M, Mezger M, Scherf U, Floudas G. What determines the glass temperature and dc-conductivity in imidazolium-polymerized ionic liquids with a polythiophene backbone? *Macromolecules* 2020;53:3535-50. [DOI](#)
67. Paluch M. Dielectric properties of ionic liquids. Switzerland: Springer; 2016. [DOI](#)
68. Wojnarowska Z, Paluch M. Recent progress on dielectric properties of protic ionic liquids. *J Phys Condens Matter* 2015;27:073202. [DOI](#) [PubMed](#)
69. Griffin P, Agapov AL, Kisliuk A, et al. Decoupling charge transport from the structural dynamics in room temperature ionic liquids. *J Chem Phys* 2011;135:114509. [DOI](#)
70. Musiał M, Cheng S, Wojnarowska Z, Paluch M. Magnitude of dynamically correlated molecules as an indicator for a dynamical crossover in ionic liquids. *J Phys Chem B* 2021;125:4141-7. [DOI](#) [PubMed](#) [PMC](#)
71. Bergman R. General susceptibility functions for relaxations in disordered systems. *J Appl Phys* 2000;88:1356-65. [DOI](#)
72. Kremer F, Schönhalz A. Broadband dielectric spectroscopy. Berlin: Springer; 2002. [DOI](#)
73. Floudas G. 2.32 - Dielectric spectroscopy. In: Matyjaszewski K, Möller M, editors. *Polymer science: a comprehensive reference*. Amsterdam: Elsevier; 2012. pp. 825-45. [DOI](#)
74. Ngai KL, Floudas G, Plazek DJ, Rizo AK. Amorphous polymers. In: Mark HF, editor. *Encyclopedia of Polymer science and technology*. New York: John Wiley & Sons; 2002. [DOI](#)
75. Adam G, Gibbs JH. On the temperature dependence of cooperative relaxation properties in glass-forming liquids. *J Chem Phys* 1965;43:139-46. [DOI](#)
76. Donth E. The size of cooperatively rearranging regions at the glass transition. *J Non Cryst Solids* 1982;53:325-30. [DOI](#)